Study Summary
Stereo X-Ray Corona Imager Mission

Yohkoh X-ray videos have dramatically shown us that the solar corona evolves dynamically on many spatial and temporal scales. But studies of the three-dimensional structure and dynamics of the solar corona have been severely limited by the constraint of single view point observations. Ambiguities in single line of sight images of the optically thin corona often make it difficult to interpret the observations. The Stereo X-Ray Coronal Imager (SXCI) mission will send a single instrument, an X-ray telescope, into deep space expressly to record stereoscopic images of the solar corona. The SXCI spacecraft will be inserted into a ~1 AU heliocentric orbit leading Earth by up to 25° at the end of the first year. **The SXCI X-ray telescope forms one element of a stereo pair, the second element being an identical X-ray telescope in Earth orbit placed there as part of the NOAA GOES program,** which is committed to continuous imaging of the solar X-ray corona beginning in 2000.

The scientific goal of the Stereo X-ray Coronal Imager (SXCI) mission is to solve two of the most fundamental problems in solar physics:
- What causes explosive coronal events such as Coronal Mass Ejections (CMEs), prominence eruptions and eruptive flares?
- What causes the transient heating of coronal loops?

Both eruptive events and transient coronal heating are thought to result from the release of energy stored in coronal magnetic fields. The release of energy results from, and produces, three dimensional changes in the coronal magnetic field that have not and cannot be revealed by single viewpoint observations. X-ray emission is a powerful diagnostic of the structure of the corona and its magnetic fields and the resulting high cadence stereoscopic X-ray images provided by these two spacecraft will reveal, for the first time, the dynamic behavior of the solar corona in three dimensions. Much information on the 3D structure and dynamics of the corona can be obtained from the stereo images alone. Stereoscopic views of structures in the optically thin corona will resolve some ambiguities inherent in the interpretation of single line-of-sight observations. Triangulation gives 3D solar coordinates of features which can be seen in the simultaneous images from both telescopes. As part of this study, tools were developed for determining the 3D geometry of coronal features using triangulation. To obtain the maximum scientific benefit from a stereo mission with only two spacecraft, the X-ray images will be supplemented with data from other near-Earth observations. In particular, magnetic modeling of the corona using measured photospheric fields will be an important analysis technique for the SXCI mission and a prototype tool for routine magnetic analysis was also developed as part of this study. Advanced technologies for visualization and analysis of stereo images were also tested for this study.

Both data analysis studies and spacecraft trade studies indicated a drifting, rather than fixed angle, orbit was preferable for the SXCI mission. The mission chosen for this study uses a Pegasus XL launch vehicle to put the SXCI spacecraft into a ~1 AU drifting orbit which reaches 25° after 9 months and dwells at this angle for 160 days. Our studies concerning the optimum stereo angle for obtaining 3D information indicate that this is a large enough angle to achieve the mission science objectives and costs are minimized by limiting the mission to 16 months. The X-ray telescope on the SXCI spacecraft would be a clone of the GOES telescopes. The SXCI spacecraft designed has a data rate of 70 kbps at 0.45 AU using 34m DSN X-band stations. Reasons for selecting X-band over Ka-band are presented. The data handling strategy involves use of a large on board storage capacity (22 Gigabits) coupled with use of daily images from the GOES instrument to determine what portion of the stored high cadence images would be selectively downlinked.

In addition to providing a wealth of new scientific information, the dynamic stereo images will provide a tremendous tool for outreach and education as evidenced by the spectacular appeal of the Yohkoh and SoHO videos. Stereo images and videos would be produced for 3D viewing using electronically shuttered liquid crystal goggles which will soon become a standard PC add-on because of their use in the computer gaming industry. Moreover, we envision 3-D IMAX movies of the X-ray corona.

Report on New Mission Concept Study

Stereo X-Ray Corona Imager Mission

Table of Contents

1. Introduction

In 1996, NASA issued a call for proposals for studies of new mission concepts for space physics (NRA 96-OSS-03). One concept selected was a Stereo X-Ray Corona Imager (SXCI) mission and this report documents the results of that study.

The goal of the SXCI mission is to make the first stereoscopic observations of the X-ray corona in order to study, in three dimensions, the structure and dynamics of the corona and its magnetic fields. In this mission, a spacecraft carrying a single instrument, an X-ray telescope, is launched into a orbit at ~1 AU leading Earth by 25° at the end nine months. The soft X-ray telescope would be identical to the soft X-ray telescope that will already be in geosynchronous orbit on-board a NOAA GOES-series weather satellite and **the two instruments will be used together to form a stereo pair.**

X-ray emission is a powerful diagnostic of the corona and its magnetic fields. Three dimensional information on the structure and dynamics of the corona would be obtained by combining the data from the two X-ray telescopes. Using the three-dimensional information from this mission, one can address the questions of what causes explosive coronal events such as coronal mass ejections (CMEs), eruptive flares and prominence eruptions and what causes the transient heating of coronal loops. Both eruptive events and transient heating are generally thought to result from the release of energy stored in stressed coronal magnetic fields. To obtain the maximum scientific benefit from a stereo X-ray mission, the stereo X-ray observations will be supplemented with magnetic modeling of the corona using measured photospheric magnetic fields to better understand the build up and release of energy in the coronal magnetic fields.

This mission study includes the scientific rationale and goals and results from mission and spacecraft design studies. A low-cost 420-day mission which samples a range of stereo angles was baselined and costed. In addition, studies were made of data analysis techniques and technologies for obtaining the necessary 3D information from only two simultaneous viewpoints. Several tools for this analysis were developed and tested on simulated stereo data created from solar rotation using both Yohkoh/SXT and SoHO/EIT data. An example of a rotational stereo Yohkoh/SXT pair is shown on the cover; here the separation is about 5 hours, corresponding to a stereo angle of about 3°. Fig. 1-1 shows four rotational stereo pairs of SoHO/EIT data from each of EIT's four wavelengths. (The left and right eye images are 6 hours apart; for each eye, the 4 wavelengths were taken within minutes of each other.) Such SXT and EIT observations were also used to explore and develop advanced technologies for the display and analysis of stereoscopic data including 3D viewing of stereo images using liquid crystal shuttered goggles and stereoscopic High Definition Television (HDTV). Dynamic stereo images and videos from such a mission can be used for both science analysis and outreach/education.

2. Science Rationale and Objectives

The Earth travels through the extended atmosphere of a magnetically active star, our Sun. The Sun's outer atmosphere, the corona, is a dynamic million degree plasma extending outward from the 6000 K solar surface, the photosphere. The energy for heating the corona and solar wind is supplied by magnetic fields which are generated deep within the Sun by the solar dynamo and emerge through the photosphere. The buildup and release of magnetic energy in the corona is accompanied by changes in the three-dimensional structure of the corona and its magnetic fields which can not be determined from single viewpoint observations. The uncertainties in interpreting the integrated single viewpoint line-of-sight

observations of the optically thin corona are frequently so great that a significant understanding of the observed coronal structures and processes is not possible.

The most dramatic solar events are Coronal Mass Ejections (CMEs), prominence eruptions and solar flares. These explosive energy releases can cause geomagnetic storms and energetic particle events at Earth with harmful effects on spacecraft hardware, humans in space, communication and navigation systems, and electrical power grids. CMEs, the largest of the explosive events, are enormous (10^{15}-10^{16} g) bright masses of coronal material which move out from the Sun at up to 2000 km/s. They are thought to be the cause of the most severe space weather events, e.g., the largest geomagnetic storms and energetic particle events. The geomagnetic storms result when the CME impacts the Earth's magnetosphere. Solar flares also generate energetic particles which are a major factor in space weather. The most damaging particle events, however, are thought to be associated with interplanetary shocks driven by the fastest CMEs. Eruptive coronal events are generally thought to result from the release of energy stored in stressed coronal magnetic fields. To be able to predict these space weather events, one must understand the origin of these eruptive releases of magnetic energy in the corona.

Top priorities in the study of the physics of the solar wind and heliosphere identified in the NRC's *Science Strategy for Space Physics*, (1995, p. 3) include to "Carry out stereo imaging of the solar corona to reveal the three-dimensional structure of coronal features without the ambiguity caused by integration along the line-of-sight," and to "Develop and use techniques for the remote sensing of the coronal magnetic field in order to improve knowledge of the acceleration of the solar wind and of the initiation of coronal mass ejections." Both priorities are addressed in this Stereo X-ray Corona Imager mission and study.

The scientific objectives of this mission require a determination of the three-dimensional structure of the corona and its magnetic fields and how they evolve in time. The two major objectives are

(1) What causes explosive coronal events such as CMEs, eruptive flares and prominence eruptions?

The key to understanding the origin of CMEs and other eruptive events will be observations that allow us to determine in three-dimensions the structure and evolution of the corona and its magnetic fields before, during and after the events.

(2) What causes transient coronal loop heating?

It is not understood why only certain loops in the closed field regions of the corona are heated and filled with plasma while others are not. Determination of the 3-D geometry of the loop will allow us to constrain theories of loop heating and to relate the heating to photospheric phenomena, interactions with other magnetic flux systems, and structural changes in the loop.

Stereoscopic X-ray data are essential to obtaining the necessary 3-D information on the structure and dynamics of the corona needed for these objectives. The corona is a million degree plasma that radiates strongly in X-rays, the intensity of the emission being

proportional to the square of the plasma density. However, since the magnetic field pressure in the corona is generally greater than the plasma pressure, the magnetic field restricts the motion of the plasma, forcing it to follow the magnetic field lines. Since only magnetic field lines which hold hot ($>10^6$ K) plasma radiate, the X-ray emission directly traces those coronal magnetic field lines with heated plasma.

Table 2-1. Major Scientific Objectives

- Determine the cause of explosive coronal events such as coronal mass ejections (CMEs), eruptive flares and prominence eruptions.

- Determine the cause of transient coronal loop heating.

Table 2-2. Specific Objectives from Stereo X-ray Data Alone
(0-40° Stereo Angle)

- Determine definitively if there are interacting coronal loops causing loop heating. The stereo observations will identify unambiguous points of enhanced emission and determine whether the emission is due to enhanced heating/density or line-of-sight effects.

- Determine the three-dimensional geometry of coronal structures, e.g., loops, coronal hole walls, helmet streamers and CMEs. From time sequences, determine the speeds and direction of motion of features that can be identified in both images. Use to analyze the 3D evolution of the corona during eruptive events as well as transient loop heating.

- Determine the photospheric footpoints of coronal loops by downward extrapolation. Study the importance of photospheric velocity, photospheric magnetic fields and flux emergence to heating coronal loops.

- Study the role of the dark cavity in CMEs and consequently the possible role of magnetic buoyancy and gravity in CME initiation. Lack of a dark cavity in single viewpoint observation of a pre-CME configuration may be a line-of-sight effect.

- For CMEs viewed along the arcade axis, look for closed field lines around the CMEs to determine if reconnection in the low corona precedes CME initiation. Theories vary as to whether reconnection proceeds or follows CME lift-off and whether the reconnection occurs low in the corona (below the flux rope) or higher in the corona (above the arcade).

Many questions relating to the science objectives can answered with the stereo X-ray observations alone (Table 2-2 and Sec. 2.B below). For maximum scientific benefit, the stereo X-ray data can be supplemented with other solar observations as available from ground based observatories and spacecraft such as SoHO or Solar B. Specifically, supplementing the X-ray observations with magnetic models of the corona extrapolated from magnetograms will considerably enhance our understanding of the 3D evolution of the coronal magnetic fields and the energy stored in them. The fraction of the total magnetic energy that is available to heat the corona and to power dynamic phenomena is stored in the

component of the field that determines the coronal currents, the non-potential component. Using force-free magnetic field models (see McClymont et al 1997 and references therein) computed from daily vector magnetograms and constrained by the stereo observations will allow us to quantify the non-potential component of the magnetic field and show how the stored energy builds up with time and how it is released (in transient or eruptive events) or how it decays. Scientific objectives which can be achieved using both X-ray and vector magnetogram data are described in Table 2-3.

Table 2-3.   Specific Objectives from Stereo X-ray Data plus Magnetic Field Models (0-40° Stereo Angle)

- Determine the 4D (3 spatial dimensions plus time) evolution of the magnetic field configuration accompanying eruptive events and heating using force-free models of the coronal magnetic fields with measured photospheric fields as boundary conditions. Specifically, quantitatively analyze roles of photospheric velocity shear, and flux emergence in CME initiation. Use to constrain theoretical models of such.

- Determine the non-potential component of the field to determine energy build up and release accompanying eruptive events and heating using force-free models of the coronal magnetic fields with measured photospheric fields as boundary conditions. Use to constrain theoretical models of such events. Determine deviations from force-free fields indicating role of pressure and/or gravity.

- Determine the photospheric footpoints of coronal loops by identifying field lines in stereo observations with field lines in magnetic field models. Analyze the importance of photospheric velocity, photospheric magnetic fields and flux emergence to heating coronal loops.

The primary mission of this study lasts 460 days and covers stereo angles in the range 0-25°; this was determined to be sufficient to meet the above major scientific objectives (Table 2-1) as well as specific objectives (Tables 2-2 and 2-3). However, the orbit chosen for this study was a drifting (not fixed angle) orbit such that by 18 months, a separation of 50° is reached. At these larger separation angles, additional scientific objectives can also be achieved (Table 2-4).

Table 2-4.   Specific Scientific Objectives for Extended Mission (>40° Stereo Angle)

- Study evolution of coronal features for longer time scales made possible by extended longitudinal X-ray coverage of Sun provided by the two X-ray telescopes.

- Study evolution of X-ray corona for regions of Sun underlying CMEs seen on the limb from near-Earth coronagraphs.

2.A Limitations of a Single Viewpoint and Need for Stereo X-ray Observations

The X-ray and EUV images from the Yohkoh and SoHO missions have provided many exciting results on the structure and dynamics of the solar corona. However, like all single vantage point observations, the images are often ambiguous in their interpretation.

Understanding both a coronal loop's geometry and the photospheric location of its footpoints is important for understanding the loop's heating and its relationship to photospheric phenomena. Single viewpoint observations of an isolated coronal loop are insufficient to determine the 3D loop geometry because the angle that the loop makes with respect to the plane of the sky is not known. One cannot extrapolate a loop reliably from the point it disappears in the lower corona to the photosphere unless the angle with respect to the plane of the sky is known.

Interpretation of single line-of-sight observations is further complicated by the fact that the coronal structures are optically thin at X-ray wavelengths. Coronal loops, and the larger structures that they comprise, are not in general isolated. Other structures often lie along the line-of-sight, either in front of or behind the structure of interest causing a "background" problem (Fig. 2-1). With only a single viewpoint, it is often difficult, if not impossible, to disentangle the various structures that overlap along a single line-of-sight within an image.

Fig. 2-1. Illustration of the "background" problem. The observed emission is integrated along the line of sight through the optically thin corona.

Many Yohkoh images show loops apparently interacting with adjacent loops. But without a stereo view point, it is not possible to resolve the ambiguity of whether the brightenings of the loops are a result of summing intensities along the line of sight or if the loops physically interact. In some eruptive event scenarios, the energy release is triggered by the interaction of neighboring flux systems. But a close neighbor in a 2-D view may be quite distant when the third dimension is considered (Fig. 2-2). Thus it is essential to have the stereo observations of the X-ray/EUV corona to resolve such ambiguities in the interpretation of changes in the coronal structure.

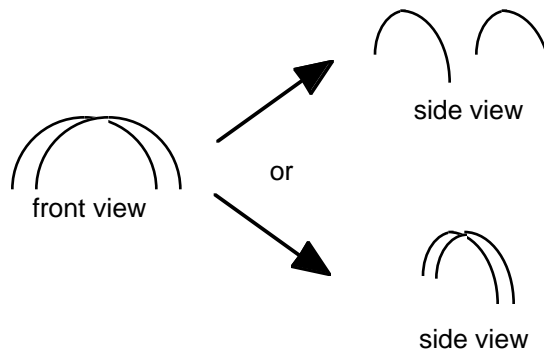**Fig. 2-2. Illustration of the "interacting loop" problem.** Loops that appear to be touching in one view may be widely separated when viewed from another angle.

Most theories of the origin of eruptive events including CMEs and eruptive prominences involve changes in the three-dimensional geometry of the corona which can not be determined from single view point observations. For example, several theories involve

arcades overlying filaments and filament channels. A dark cavity may surround the filament. A build up of magnetic energy from photospheric flows, flux emergence, reconnection below the filament or magnetic buoyancy may cause the eruption. Single view point line-of-sight observations do not give us enough information about the evolution of the coronal fields to distinguish between various models. For example, lack of a dark cavity in a single viewpoint observation may be a line-of-sight effect.

2.B Origin of Eruptive Coronal Events

Understanding Coronal Mass Ejections, prominence eruptions and eruptive flares is one of the most important problems in solar physics because of their major roles in coronal evolution and space weather (see, e.g. Gosling, 1993). Despite their importance, they are poorly understood. Recent SoHO/LASCO and EIT results have only compounded the problem because of the discovery that CMEs occur much more frequently and on a wider range of spatial scales than previously observed. Basic open questions about CMEs and other eruptive events include

- Is the driving energy source purely magnetic or does gravity play a role?
- What is the pre-event geometry or geometries?
- What is the role of magnetic reconnection?
- What is the role of evolving surface features and/or emerging flux?
- What is the role of kink instabilities and helicity?

CMEs are known to frequently occur under helmet streamers; the streamer is sometimes observed to swell for several days prior to the eruption, suggesting a build up of stress in the corona. Often, but not always, a filament eruption accompanies the CME. The filaments may also become "activated" prior to the eruption.

Several theories of CMEs and filament eruption are based on a bipolar arcade geometry consistent with the above observations: A magnetic arcade overlies a neutral line. In some theories, this arcade includes a dark cavity within which a filament is located. The filament overlies the neutral line and it may have a helical field or be twisted (S or reversed S). Many scenarios for eruptions involve increasing the stored magnetic energy by stressing the fields through footpoint motion driven by photospheric flows. In some models, the arcade footpoints are sheared resulting in an expansion of the loops; eruption results when some critical shear level is reached (e.g., Mikic & Linker, 1994). In other scenarios, the field is stressed by converging photospheric flows which bring opposite polarity fields to the neutral line whereupon they reconnect. A coronal flux rope or filament, created by the reconnection, steadily grows with time. In some circumstances a loss of equilibrium may eventually occur and this could result in a full eruption (e.g., Isenberg, Forbes, & Demoulin 1993). In other scenarios, interaction of the arcade-prominence system with an emerging flux system is responsible for the eruption (Feynman and Martin 1995). A kink instability (Pevtsov et al., 1996; Rust and Kumar, 1994) or reconnection between existing loops (Moore et al, 1997) are also candidates for triggering the eruptive event.

These and other scenarios can be tested with stereo observations. For example, stereo observation will determine whether the CME geometry is essentially 2D (similar to the infinite arcade assumed in many of the theoretical models), or fully 3D. In addition, the role of reconnection varies in the models. Several models require reconnection below the flux

rope (or during the flux rope formation) to initiate the eruption. This implies that closed magnetic loops form and these should be visible in the stereo X-ray observations if the arcade is viewed along the arcade axis ("end on."). However, often no closed loops are observed and there is considerable evidence that field lines seem to remain open for a considerable time after an eruption has begun. While this seems to contradict the reconnection trigger theories, ambiguity in the single line-of-sight observations leave this an open issue.

Although most theories involve magnetic energy, some invoke gravitational energy. The frequent presence of a dark cavity in CMEs suggests that a magnetic buoyancy instability (and thus gravitational energy) causes the CME. If a pre-CME configuration does not have a dark cavity (indicating a region of reduced plasma density), then magnetic buoyancy can be ruled out. However, a cavity might not be seen in a single line-of-sight observation because of bright material in the foreground or background. Thus stereo X-ray observation will determine the role of the cavity and magnetic buoyancy in CME initiation.

Other theories invoke geometries quite distinct from the bipolar arcades discussed above. Stereo observation will be able to distinguish these magnetic configurations from bipolar arcade configurations. In some scenarios, the "collision" of two neighboring flux systems and the resulting reconnection triggers the eruption. Recently, Antiochos (1997) has proposed a scenario based on a initial quadrapole magnetic geometry. In the quadrapole scenario, reconnection occurs first high in the corona above the closed loops which become the CME; thus reconnection precedes CME liftoff. Stereo X-ray observation should be able to test this theory by determining whether reconnection occurs above the CME before the eruption or below the flux rope after the CME liftoff as in several arcade theories.

Clearly, knowledge of the 3D magnetic field configuration before, during and after eruptive events is necessary to constrain theories and understand the causes of eruptive events. If the magnetic field configuration is determined accurately enough, the evolution of the stored energy and the 3D field topology can be followed and theories tested against the observations. The fraction of the total magnetic energy that is available to heat the corona and to power dynamic phenomena is stored in the component of the field that determines the coronal currents, the non-potential component. One goal of the SXCI mission will be to create magnetic models extrapolated from measured photospheric fields and consistent with the stereo X-ray images. Force-free magnetic field models (McClymont et al., 1997; Mikic and McClymont, 1994), i.e. models which allow currents only parallel to the magnetic field, are a good approximation for computing non-potential fields. Using the force-free magnetic field models consistent with the X-ray and magnetic field data, we can identify the non-potential component and show how it builds up with time and how it is released, in transient or eruptive events, or how it decays. In this way, the build up and release of magnetic energy causing the eruptive and heating events can be determined. If force-free models consistent with both the photospheric fields and the X-ray observations cannot be found, then the force free model may be inadequate, implying the importance of gravity and/or thermal pressure. If these forces are also important, then only full MHD models may adequately describe the dynamics.

The study of the origins of CMEs would benefit from extending the mission to stereo angles of greater than 40°. The one certain early diagnosis of a CME is its detection in a white-light coronagraph and our best views of CMEs are those near the limb. CMEs from

the disk are difficult to diagnose in a coronagraph because of much brighter solar background; only when the CME has expanded and become much larger than the Sun (and thus well after liftoff) can it be observed in white light as a "halo" CME. SoHO/LASCO has observed a number of such halo CMEs, but because of the delay in observing halo CMEs, it is frequently not possible to determine the corresponding coronal activity observed in EUV (SoHO/EIT). Presently, we only observe the X-ray corona on the front of the Sun. At larger stereo angles, the SXCI X-ray telescope will begin to see the regions of the corona underlying the near-limb CMEs allowing the same CME to be observed from its creation in the low corona to its ejection into interplanetary space. This will allows us to identify unambiguously the activity in the X-ray corona that precedes the CME. Larger stereo angles also provide increased longitudinal coverage of the X-ray Sun allowing one to follow the evolution of active regions and other features for longer periods of time.

2.C. Transient and Steady Coronal Heating

The corona is completely filled with magnetic flux. Distinct plasma loops exist only because of spatial variations in the rate of energy input. Flux tubes that are strongly heated are hot and dense (and thus visible in X-rays); heat flows down the flux tube, evaporating the high density photospheric plasma which expands to fill the flux tube. Flux tubes that are weakly heated are cool and tenuous. The physical mechanism responsible for the heating and the reason for its spatial variation are long standing and fundamental questions. A number of interesting ideas have been proposed, including the dissipation of electric currents associated with magnetic stress (possibly involving magnetic reconnection) and the dissipation of MHD waves generated in the photosphere or low corona. Microflares, jets and emerging flux may all play a role. However, none of the proposed models has been convincingly demonstrated to be correct. Stereoscopic observations have the potential to provide valuable new information that will greatly improve our understanding of both steady and transient coronal heating. Several examples of how stereo X-ray observations might lead to progress are given below. However, because of the limited resolution of the X-ray telescopes baselined for this study (~5 arcsec for 512x512 CCD and ~2.5 arcsec for 1024x1024 CCD), while variations in emissivity along the loop length can be observed, any variations across the cross-section cannot be resolved. Thus, for the X-ray telescopes baselined, we concluded that only the transient heating of loops can be studied by this mission. Based on Yohkoh observations, X-ray telescopes with ~1 arcsec resolution are probably needed to resolve loop cross sections and address the issue of steady-state loop heating.

Most loops observed by Yohkoh appear to be slowly varying in relation to conductive and radiative cooling times, and it is reasonable to suppose that the loops are maintained in a quasistatic equilibrium by a steady or quasisteady heat source (e.g., Porter & Klimchuk, 1995). The theory of quasistatic loop equilibrium has been carefully worked out since the time of Skylab (e.g. Rosner, Tucker, & Vaiana, 1978; Craig, McClymont, and Underwood, 1978; Vesecky, Antiochos, & Underwood, 1979). One of the most basic properties of equilibrium loops is that temperature, density, and pressure are all nearly constant throughout the coronal portion of the loop. Significant variation occurs only in the lower portion of the legs. In contrast with the theory, Yohkoh observations often indicate considerable variation along much of the loop axis (e.g., Kano & Tsuneta, 1996). If this variation is real, it is has important implications for both the heating and dynamics of loops (e.g., Klimchuk, 1992). The extent to which the Yohkoh variations are real is unclear,

however. A major difficulty has been the lack of accurate information on the line-of-sight thickness of the emitting plasma. This thickness is required in order to determine density and pressure from the observed intensities. In the case of loops, it is customary to infer the thickness by assuming that the cross section is circular and that the axis is oriented at a particular angle to the line of sight. Both assumptions are a potential source of significant error. The orientation is especially critical, since the plane of a loop can have any inclination relative to vertical, and furthermore many loops do not lie within planes. The stereo observations will be able to determine the orientation of the loop plane and thus improve these estimates.

It has been demonstrated that the ambiguities associated with unknown line-of-sight effects can have a sizable impact on the interpretation of Yokoh data (Alexander & Ketsev, 1996; Forbes & Acton, 1996). Stereo observations will of course eliminate these ambiguities and allow for a much more accurate determination of loop densities and pressures. We will thus be able to investigate the detailed variations of temperature, density, and pressure along the axes of loops, which will give us a much better understanding of loop heating and dynamics. In addition to studying the detailed properties of individual loops, it is useful to study the global properties of many loops and to search for statistical relationships. These relationships are often referred to as scaling laws. Several scaling laws have been derived from the Yohkoh data (e.g., Kano & Tsuneta, 1995), and two that are particularly revealing concern the statistical dependence of pressure and temperature on loop length (Klimchuk & Porter, 1995; Porter & Klimchuk, 1995). The results imply that, for quasisteady heating, the heating rate scales inversely with the square of the length. This places a valuable constraint on theories of coronal heating, which make different predictions about what the scaling should be. Parker's (1983, 1988) idea of the wrapping and braiding of coronal field lines due to random translational motions of the footpoints seems to be most consistent with the data. However, these and all scaling laws derived from single vantage point observations are susceptible to line-of-sight ambiguities. This causes uncertainties in the measured density and pressure, as described above, as well as uncertainties in the measured loop length. Loop lengths are generally determined by assuming that the loop lies flat on the solar surface or that the loop has a perfect semi-circular shape. Both assumptions are obviously gross approximations to reality, and it is unclear how they may impact the derived scaling laws. Stereo observations will eliminate these uncertainties.

Although most Yohkoh loops appear to be steady in relation to relevant physical time scales, there are many that clearly are not. Some active region loops that are especially short lived have been given the name "transient loop brightenings" (Shimizu, 1992). Detailed analysis of these structures reveals that they are usually comprised of multiple loops, and that the initial brightening occurs at an apparent point of contact between adjacent loops (Shimizu et al., 1994). Whether the loops are actually in contact and interacting with each other is rather speculative at this point. The observed brightenings could be due to enhanced temperatures and densities that would result from an impulsive energy release, or they could be simply due to a line-of-sight integration effect. Only stereo observations will be able to answer this question, as illustrated in Fig. 2-2.

3. Determining the 3D Structure of the Corona from Analysis of Stereo X-ray Data

Here we discuss techniques to extract quantitative information on 3D structure and dynamics from just two simultaneous view points and discuss the implications for the choice of stereo viewing angle.

3.A Determination of 3D Solar Coordinates from Triangulation of Stereo Pairs

It has not been generally appreciated that quantitative information on the 3D magnetic fields can be found by using "triangulation" or "surveying" of coronal loops and features observed from two simultaneous views (i.e., from two spacecraft). Using classic surveying techniques, the solar coordinates in *three-dimensions* of a coronal "feature" can be determined from only two simultaneous views as long as (a) one knows the angular separation of the two views and the spacecraft-Sun distances and directions and (b) one can recognize the "feature" in both images. This technique was used by Berton and Sakurai (1985) on Skylab loops and on simulated loops by Gary et al. (1997b). The use of triangulation to determine the 3D magnetic structure from two views is limited to features easily identified in both images and this can be a serious limitation. For features which can be identified, this technique can be used to trace out the feature, and thus the magnetic field lines, in three-dimensions.
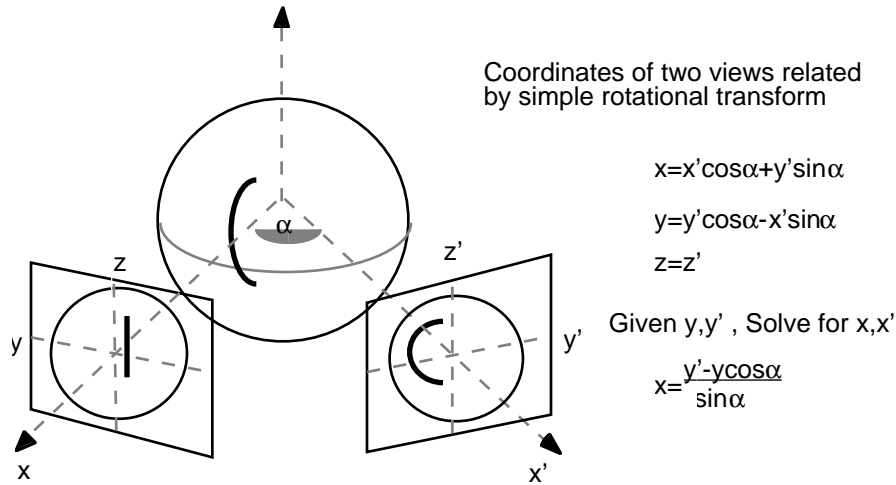
Fig. 3-1. Determination of coronal loop height via triangulation. Coronal loop as seen from two view points separated in the ecliptic by stereo angle α. The coordinates in the plane of the sky for the two views are related by a simple rotational transform and the complete 3D geometry of the loop can be determined from the measured (x,y) and (x',y') as shown.

The triangulation technique for a simple case is shown schematically in Fig. 3-1 where it is assumed that both views are from the equatorial plane of the Sun. In this figure, the coordinates in the plane of the sky of the two views with stereo angle α are related by the simple rotational transform

$$T(\alpha) = \begin{pmatrix} \cos\alpha & \sin\alpha & 0 \\ -\sin\alpha & \cos\alpha & 0 \\ 0 & 0 & 1 \end{pmatrix}.$$

As part of this study, we have developed two analysis tools which use triangulation to determine the 3D coordinates of coronal features. These tools have been developed using simulated stereo pairs formed using solar rotation and tested on true stereo pairs made using simple known loops. Using either tool, the user identifies and marks the location of the same coronal feature in both images of a stereo pair. The two points located in this way are called "tiepoints." The tool writes the pair of (i,j) coordinates (in pixels) of the feature tiepoints into an ASCII tiepoint file. For both tools, a separate program XYZSUN computes the 3D solar coordinates of the point from the tiepoints. These tools have been developed for the general case where the solar rotation axis is at an arbitrary angle with respect to the optical axis. In this general case, the transformation matrix involved becomes more complicated than the simple single-axis rotation matrix $T(\alpha)$ shown above.

The tiepoint files can be created with either of two tools. The first method for creating tiepoints, illustrated in Fig. 3-2, uses the commercial software package ENVI which runs under IDL. Figure 3-2 shows the screen output from an ENVI session tiepointing features in two EIT Fe IX/X images taken 6 hours apart. The three windows for each image show the image at different magnifications and are used to select different regions of the image for tiepointing. The actual tiepointing is done in the two "Zoom" windows (whose magnification can be varied) in which the red cross hairs are used to locate the same feature in both images. When the user has located both sets of cross hairs on the same feature, he hits the "add point" button and the pixel coordinates of the two points are added to the tiepoint file. (The use of XYZSUN and the ENVI tool for the loop in Fig. 3-2 gave a loop height of approximately 100,000 km with about a 30% error.)

The second tool for tiepointing, called the 3DCursor, utilizes true stereoscopic "three-dimensional" visualization on Silicon Graphics workstations which support stereo visualization using an interlaced screen and electronically shuttered goggles. The liquid crystal goggles shutter between left and right eyes coherently with the screen sweeping the left and right eye images so that each eye sees only one image and the user sees the image in stereo 3D (This technology and other advanced visualization technologies are discussed in Sec. 4). Using the 3DCursor tool, the user can move a tiepoint in all three dimensions, placing it on features as seen in his 3D stereo view. Thus as he moves the cursor in the z-direction (perpendicular to the screen), the cursor seems to move in and out of the Sun. In reality, the separation of the cursor location on the left and right eye images is changing, making the cursor appear to move in and out in the stereo view. Once the cursor is located on a feature, the user adds this point to a tiepoint file. Since the 3DCursor program is actually moving two tiepoints, one in the right eye image and one in the left eye image, this tool determines the (i,j) coordinates of a feature in both images just as does the first tool. Tiepoint files created using ENVI can also be read into the 3DCursor tool (and vice versa) and viewed in stereo.

A separate code, XYZSUN, takes the tiepoints and uses triangulation to compute the 3D location of the features in solar coordinates (Solar radius, latitude and longitude) using user inputs and the JPL NAIF-SPICE solar system ephemeris (Lorre et al., 1997). XYZSUN works by first determining the coordinate transformation (rotation matrix plus Sun-spacecraft vector) between the telescope frame of reference and the solar coordinate system. (It currently assumes that the spacecraft is in Earth-orbit since at present we have only rotational stereo data, but can be modified to use the spacecraft orbits for a stereo mission.)

Using the time at which each image was taken, XYZSUN uses the ephemeris data to determine the solar longitude and latitude of the sub-solar point of the spacecraft and the distance from the Sun to the spacecraft. XYZSUN also needs information on the telescope focal length and the location of the optical axis on the image (in pixels) to be able to transform between image coordinates (pixels) and solar coordinates. The tiepoint from each image of a pair determines a ray tracing backwards from the image plane towards the Sun. If there were no errors, the two rays would intersect at the location of the tiepointed feature. However, errors are introduced by the spacecraft, the telescope and the tiepointing itself. Therefore XYZSUN actually computes the point of closest approach (in solar coordinates) of the two rays and the location of the feature is taken to be midway between the two rays at closest approach. The program also has a manual mode for use with simulated data or with data where ephemeris and/or focal length data are not available and this mode was used to test the code on simple 3D loops with known coordinates. A stereo image pair was created by rendering images of the loops from two angles separated by 15°; this image pair is shown in Fig. 3-3. A tiepoint file of points lying on these loops was created using the 3DCursor tool and the 3D coordinates of these points were then computed by XYZSUN and compared with the known coordinates. Shown on the right in Fig. 3-3 are the (x,y,z) location of points (X's) determined in this way plotted over the known test loops (solid lines); agreement is excellent.

Various sources of error contribute to uncertainties in the solar coordinates of a feature computed from the tiepoints. Errors in the alignment of the images, in the location of the optical axis on the image and in the vector from the spacecraft to the Sun center will all contribute to errors in the final solar coordinates. These errors can be minimized and the largest source of error is most likely to be in the determination of the tiepoints themselves due to differences in the appearance of the "feature" in the two images or due to the fuzziness of the feature itself. The accuracy also depends strongly on both the resolution of the image itself and the stereo angle. Referring to Fig. 3-1, alignment, identification and resolution would contribute to errors in determining the coordinates (y,z) and (y',z'); call this error Δy. The error introduced into the determination of the coordinate in the third direction (x, x' in Fig. 3-1) by the error Δy depends on the stereo angle via the transformation. This error is $\Delta x \sim \Delta y/\sin\alpha$ where we have used the transformation $x=(y'-y\cos\alpha)/\sin\alpha$ (Fig. 3-1). This shows that the overall error in determining the 3D coordinates of a feature is larger than the error in locating the tiepoints by $1/\sin\alpha$ and thus reasonably large stereo angles are needed for accurate 3D coordinate determination. For example, a stereo angle of 5° leads to a multiplication of the error Δx by $1/\sin\alpha = 11.5$ and the overall error in the 3D location of the feature is increased by an order of magnitude. A one pixel error in locating a tiepoint on a 1024x1024 solar image gives an error $\Delta y/R_S \approx$ 0.25% assuming the solar radius is 400 pixels. The overall error in the 3D coordinate determination for a stereo angle of 5° is then $\Delta R/R_S \approx$ 3% or 20,000 km. If the stereo angle were 15°, the error is reduced by about a factor of 3 and $\Delta R/R_S \approx$ 1% or 7000 km. For making comparisons with magnetic field models, an error in the range $\Delta R/R_S \approx$ 1-2% is probably acceptable since magnetograms typically have errors ~10%.

The above error analysis suggests that the optimum angles would have $\sin\alpha \approx 1$. However, the most serious source of error is most likely to be the ability to identify same feature accurately in both images of the stereo pair and this fact argues for smaller stereo angles. In rotational stereo pairs, the actual changes in the corona mean that the same feature may not even be present in both images or it may have changed location. For true stereo images, the

fact that the corona is optically thin in X-rays will cause differences in a feature seen in two simultaneous images. The ability to identify and tiepoint the same feature in both images is a serious limitation of this technique and feature identification is easier for smaller stereo angles. Therefore, stereo angles in the range of 15-30° are probably optimum for analyzing the coronal structure via triangulation of features. A study by Gary et al (1997b) using simulated stereo X-ray data of loop complexes determined that the optimum angular separation was approximately 30°.

Test Loops

Tiepointing Results (X)
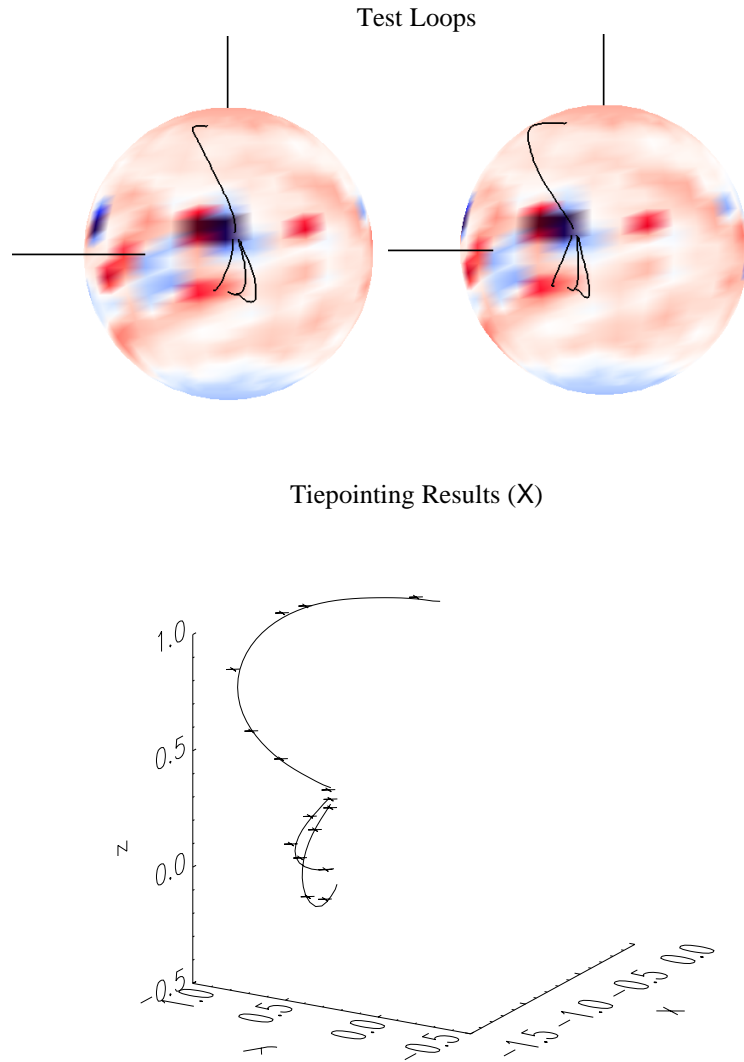
Fig. 3-3.   Test of determination of 3D loop geometry on known loops.
The test stereo image pair (top) was created by viewing the known loops from two angles separated by 15° (This pair may be viewed in stereo by relaxing your eye focus). The (x,y,z) location of points (X's) determined by triangulation from the stereo pair are plotted over the known test loops (solid curves). Agreement is excellent.

3.B Magnetic Modeling

In order to obtain more complete 3D magnetic field information and achieve the objectives in Table 2-3, it will be necessary to supplement stereo observation with 3D magnetic field

models computed using observed photospheric magnetic fields. The creation of potential or force-free magnetic field models using measured photospheric fields as boundary conditions does not require a stereo mission, of course. But the magnetic field models alone do not predict which field lines have hot plasma attached. The magnetic field models must be used in conjunction with X-ray observations so that field lines in the model can be matched to coronal loops seen in the X-ray images and the magnetic models verified. Because of ambiguities in single viewpoint line-of-sight observations, simultaneous stereo observations will allow a much better identification between features in the model and features in the observations. Loops and other features that have been determined by triangulation can also be compared to features in the 3D magnetic field model. If a correspondence between the model and observed features can be made, the magnetic field model can be validated and the model can be used to analyze the evolution of the stored (non-potential) magnetic energy.

Moreover, starting from the verified magnetic models, a complete 4D (three spatial dimension plus time) model of the corona can be built up from a time sequence of stereo images plus daily magnetograms. Each 3D model of the corona uses field lines from the magnetic model as the skeleton; plasma is "attached" to model field lines and the plasma and its emission must be modeled in such a way that the emission calculated from this model agrees with the X-ray observations from both viewpoints (see the work by Gary, 1997a). In one rigorous approach towards reconstructing the plasma-magnetic field model, Gary et al. (1997b) have shown that one can use tomography to reconstruct coronal features in three dimensions if the tomographic process is constrained using a magnetic field model.

Creating 4D models of the coronal magnetic fields and plasma consistent with the stereo observation will be difficult, but will greatly enhance the scientific return of the mission as shown in Table 2-3. These models will all use 3D magnetic field models computed from vector magnetograms. This type of analysis of the stereoscopic data will then require tools for easily creating magnetic models and comparing them with the stereo images. As part of this study, we developed a prototype user-friendly tool for computing magnetic fields from magnetograms and comparing results to stereo image pairs. This tool creates global magnetic field models from synoptic magnetogram using a potential magnetic field model (Mikic, 1997). The tool manages all the user files and creates windows to compare the 3D model results with both rotational stereo views. Results from this tool are shown in Fig. 3-4; all show the Sun viewed from the same angle. The left image is the synoptic magnetogram for Carrington Rotation 1878; the middle image shows magnetic field lines from a potential magnetic field computation using the synoptic magnetogram, and the image on the right is SXT X-ray data for January 5, 1994. Even for this simple magnetic field model, a correspondence can be seen between the model and X-ray loops. (However, there is not as close a correspondence here as between X-ray features and field lines extrapolated from the line-of-sight daily magnetograms.)

4. Advanced Technologies for Visualization and Analysis of Solar Images

The use of several advanced technologies for visualization and analysis of solar images was explored as part of this study. First, technologies for four-dimensional (4D) visualization and analysis of stereo data using both standard computer monitors and High Definition Television (HDTV) monitors are presented. Second, the exploration of software for the

automatic tracking of features in the corona is discussed. Third, the use of visualization products for education and outreach is considered. These technologies were originally adapted for the visualization and analysis of planetary phenomena by JPL's Solar System Visualization (SSV) Project and we have extended their use for the study of the Sun.

4. A Advanced Technologies for Visualization and Analysis of Sequences of Stereo Images

1. Use of Standard Computer Monitors for 4D Display of Stereo Image Pairs

The use of advanced digital technologies for the display and analysis of stereo X-ray image sequences will greatly enhance the science return from stereo missions. The human brain has adapted to extract the three-dimensional (3D) structure of objects from two-dimensional (2D) stereo image pairs. Humans can extrapolate 4D object motion and structural changes from a small sequence of images. We perceive the world through two closely spaced optical sensors which form sequences of 2D images on our retinas. A complex neural network processes these sequences to create a 4D model of our universe. This process "automatically" recognizes, classifies and separates differences in the 2D patterns. It identifies which patterns are associated with temporal and spatial changes and modifies the model accordingly. The process must properly identify whether the pattern changes are associated with object motion, structural changes, changes of viewpoint, or lighting changes.

Table 4-1. Comparison of Technologies for 3D & 4D Stereo Visualization

Device	Resolution (eyes-x-y)	Images per sec	Comments
Standard TV interlaced	1x640x480	30	data storage (video tape) analog and lossy; not suitable for archiving
Standard TV stereo interlaced	2x640x240	60	interlaced left&right eye (odd/even lines); stereo using 60 Hz synchronized electronically shuttered goggles;
Standard Computer monitor (non-interlaced)	1x1024x768	60	data storage is digital
Standard Computer monitor stereo interlaced	2x1024x384	60	interlaced left&right eye (odd/even lines) stereo using 60 Hz electronically shuttered goggles; data storage is digital
US HDTV Computer Monitor (non-interlaced)	1x1920x1080	60	data storage digital; suitable for archiving. (Also digital tape decks using 1/2" digital tape)
US HDTV stereo interlaced	2x1920x540	60	interlaced left & right eye; stereo using 60 Hz electronically shuttered goggles;
US HDTV stereo non-interlaced	2x1920x1080	120	polarized glasses & screen filter (120Hz synchronized); digital data storage; suitable for archiving.

The human visualization capability can be utilized for the analysis of the 4D structure of the corona. In Sec. 3.A, we discussed the use of one new technology for the 3D presentation of stereo data: Silicon Graphics computer monitors equipped with synchronized liquid

16

crystal shuttered glasses enable users to view stereo images. The stereo pair is displayed as two separate (odd-even) "interlaced fields." The left eye (odd lines) and right eye (even line) fields are displayed alternately at 60 Hz. The viewer wears 60 Hz liquid-crystal shuttered glasses which opaque the left and right eye alternately in synchronization with the alternating fields displayed on the monitor. This technology was used to implement the 3D cursor tool for triangulation described in Sec. 3.A. A time sequence of stereo pairs, may be examined in the same way thus enabling the evolution of coronal features to be studied. Shuttered-liquid crystal technology will soon be inexpensive and widely available because of its application to the computer gaming industry.

It should be noted that the vertical resolution of "stereo interlaced" images is one-half of "non-interlaced monoscopic" images using the same display device. The horizontal resolution is unaffected. For example, a standard SGI computer monitor has a resolution of 1024 pixels horizontally and 768 pixels vertically when used to display non-interlaced monoscopic images. When used in interlaced stereo mode, only half of the lines are available for each image and thus each image is 1024x384 which is inadequate for the display of 1024x1024 image pairs (or even 512x512 images). Standard computer monitors are compared to both standard TV and high definition TV monitors in Table 4-1. Note that standard TV can also be used in interlaced stereo mode. However the low resolution (640x240) coupled with the lossy data storage medium (NTSC analog video tape) make this an unattractive option. New Digital Television (DTV) equipment will provide additional options in the future.

The same computer technology can also be used to project stereo image sequences and stereo animations on a large projection screen. This was explored as part of this study using an Electrohome projector and a 16 foot by 9 foot projection screen located at JPL. Use of projected stereo is of particular use for the presentation of data at meetings and for public outreach.

2. Use of Stereo High Definition Television (HDTV) Computer Monitors

High Definition Television (HDTV) provides significantly higher resolution than standard computer monitors. An HDTV monitor built to the US industry digital "standards" has 1920 pixels horizontally and 1080 pixels vertically. Japanese monitors have 1920 pixels horizontally and 1035 pixels vertically. Data can be stored on any digital medium, including 1/2" digital tape. The cost of HDTV equipment will decrease dramatically as HDTV is broadcast into homes in the US. HDTV can be used for stereo viewing by interlacing left and right eye images and viewing the monitor with 60 Hz synchronized liquid-crystal goggles as described above for standard computer monitors. In this case, each images is 1920x540 which is an improvement over the 1024x384 for standard monitors. This technology was used in this study to create a stereo HDTV video using "rotational" stereo data from SXT. JPL has a small demonstration room equipped with a stereo projector described above in which the HDTV video can be displayed on a sixteen by nine foot screen in stereo to a group with each person wearing 60 Hz synchronized shuttered-goggles.

HDTV stereo images can also be displayed in a non-interlaced mode. This option provides the highest available broadcast resolution (last option shown in Table 4-1). The left and right eye images are displayed at full resolution (1920x1080) *alternately in time* with a

frequency of 120 Hz. Stereo viewing is accomplished by using 120 Hz synchronized liquid crystal shuttered glasses or placing a polarizing screen in front of the HDTV monitor which alternates the transmitted polarization at 120 Hz synchronously with the HDTV monitor display. In the latter case, the viewer wears only inexpensive polarized glasses. This technology was not explored in this study. For completeness, we note that 4D IMAX computer animations have been generated at resolutions of 4096 by 3002 pixels. The left and right eye images can be projected with different polarizations or synchronized using liquid crystal shuttered glasses. While not part of this study, the Solar System Visualization Project previously explored this technology creating several animation sequences for the 4D stereo IMAX movie "L5: First City in Space."

4.B Automatic Feature Tracking by Correlative Techniques

Understanding the dynamic evolution of plasmas and atmospheres is a fundamental problem in space science. Future solar missions will require the ability to track coronal features automatically for the analysis of the structure and dynamics of the solar corona. Automatic feature tracking (AFT) is needed for the quantitative analysis of 3D structure by triangulation. Presently, the analyst must place tiepoints by hand using, for example, the techniques discussed in Sec. 3.A. With AFT, tiepoints (features identifiable in a sequence of images) would be found and tracked throughout the sequence automatically. Not only would AFT allow determination of 3D coordinates of coronal features, but also, from the time sequence of images, the velocities and displacements of features can be determined. In this way, a detailed, quantitative analysis of the structure and dynamics of the solar corona would be possible. The output from such an analysis would be a tiepoint data base containing 3D positions and velocities of coronal features identified by the AFT software. This database could be used, for example, to study loop expansion rates and CME velocities in the low corona. Moreover, the tiepoints can be used to create 4D models of the corona as described in Sec. 3.B. Video sequences illustrating feature motion with time using velocity-based interpolation (morphing) tools could also be created.

As part of this study, we attempted to use existing AFT software on simulated "rotational" stereo data from SXT. The existing AFT package, the Windows Interface for Nominal Displacement Selection (WINDS) was developed to measure displacements in planetary atmospheres. WINDS automatically finds the same features in two or more images taken at different times or with different lighting conditions, viewing angles, or spectral bands. Interactive systems use slow and sometimes error prone human operators. Results are inconsistent when different human operators are used. With an automatic system, the error rate is constant for each type of scene, and the results are not only equal to those of an expert human operator, but are also consistent and repeatable. WINDS was designed to allow for factors which are critical to tracking solar features including the nature of the texture in the image data, the rotation of features over the measurement interval, the effect of viewing angle, and the vertical structure of the features. WINDS has been used to study planetary climate and weather. WINDS works by correlating identical or nearly identical small features in sequences of images.

We attempted to use WINDS with rotational stereo data from SXT without success. The resolution of SXT images is low both spatially and temporally. The WINDS correlator requires that features be well defined in at least a pair of sequential images. To perform automatic stereo analysis (3D triangulation) WINDS needs a time sequence of pairs of

images. Each left and right "eye" image pair should be simultaneously recorded from "viewpoints which differ by five to twenty-five degrees. Substituting images separated in time to create "rotational pseudo-stereo " pairs did not work. The features of interest changed far too much in the intervening time between images for either automatic or humans to be able to correlate similar features in an image pair.

4.C . Use of Visualization Products for Outreach and Education

The stereo images and videos resulting from this mission will provide superb tools for education and public outreach and we envision that both activities would be an important part of any stereoscopic imaging mission. Stereo images and videos could be used to inform and convey a sense of wonder to students and the public about the dynamic behavior of their Sun and to educate them about the various coronal features such as helmet streamers, coronal holes and active regions. Color stereo pairs, such as Fig. 1-1, can easily be viewed using inexpensive stereo viewers or by just relaxing your eye focus. Likewise, inexpensive red-blue glasses can be used to view stereo "anaglyphs" such as those in Fig. 4-1 and 4-2 which show rotational stereo pairs from SXT and EIT respectively. However, videos are necessary to fully appreciate the vast scope, beauty and dynamics of solar activity. As discussed in the previous section, several advanced technologies for 3D displays of stereo videos now exist and these should become widely available because of their use in the computer gaming and entertainment industries.

Electronically shuttered liquid crystal goggles for 3D viewing of interlaced stereo videos on personal computers should become relatively inexpensive because of their use in the computer gaming industry. High school level CD ROM on the corona could be produced using such stereo images for school and home viewing. Also digital High Definition Television (HDTV) with its much higher resolution in both interlaced and non-interlaced stereo mode (cf. Table 4-1) should become less expensive as HDTV begins to move into the home television market. Stereo PCs and HDTV can be used for both education and outreach. The most impressive technique for public outreach, and the one most that reaches the widest audience today, is 3D stereo IMAX. 3D IMAX theaters use either the shuttered goggle or polarized glasses technologies. Over one half of the IMAX theaters provide 3D projection capability. There are over one hundred 3D IMAX theaters world-wide and many more are under construction.

5. Mission Design, Stereo Angle and Orbit

The Stereo X-Ray Corona Imaging (SXCI) Mission requires the launch of a single spacecraft with a soft X-ray imaging (SXI) instrument into an approximately 1 AU orbit in the ecliptic plane leading or lagging Earth. The SXI would be identical to the instrument that will be in geosynchronous orbit on-board a NOAA GOES-series satellite and the two instruments would be used as a stereo pair. The GOES (Geostationary Operational Environmental Satellite) spacecraft are a continuing series of NOAA weather satellites aimed primarily at forecasting terrestrial weather. However, starting with the GOES M spacecraft, expected to be launched in 2000, all will carry an SXI to observe solar flares and other aspects of "space weather". Since one primary scientific objective of this mission is the study of eruptive solar phenomena, the stereo spacecraft should be launched either near solar maximum in 2001-2 or early in the declining phase (2003-4); at solar minimum, little activity is seen in X-rays.

A major issue addressed in this study is the choice of the stereo viewing angle, equivalent to the SXCI spacecraft-Sun-Earth angle. We considered both slightly elliptic "drifting" orbits and circular fixed-angle orbits. For either type of orbit, the SXCI spacecraft is initially placed in a slightly elliptic ~1 AU orbit; the spacecraft then separates ("drifts") from Earth at a rate determined by the ellipticity of the orbit. If a fixed-angle 1 AU orbit is desired, when the spacecraft reaches that angle, a spacecraft engine burn is necessary to circularize the orbit. Thus, a fixed angle orbit is inherently more expensive because the necessary propulsion system and fuel for the circularization maneuver must be included in the payload, and this increases the mass dramatically. The large impact on the mission for orbit circularization is discussed in Sec. 7.C.

In Sec. 3.A, results from the error analysis of 3D solar coordinate determination by triangulation from stereo image pairs led to the conclusion that angles greater than 15° were needed to obtain reasonable errors on 3D feature location. However, angles smaller than 45° are probably needed to be able to recognize the same feature in both images of a stereo pair. A separate study of the optimum angle for stereo X-ray data analysis by Gary et al. (1997b) using simulated stereo data indicated that the optimum angle lies in the range 20-40°. As part of this study, we had planned to observe long-lived X-ray features in the Yohkoh/SXT data using stereo pairs simulated by solar rotation to study feature recognition, stereo reconstruction and 3D coordinate determination for a range of stereo angles. Stereo angles of 15° correspond to lifetimes of about 27 hours. However, in a search of many months of SXT data, no well defined loops or other features were found that lasted even as long as 10 hours (~5.5°). Therefore, it was not possible to determine a preferred stereo angle for feature recognition from the existing single view point X-ray observations. It is probably not possible to determine a preferred angle until true stereo X-ray image pairs are obtained; moreover, the optimum angle may well vary with the size or type of coronal feature. Therefore, for the first stereo X-ray mission, we concluded that a wide range of angles is best.
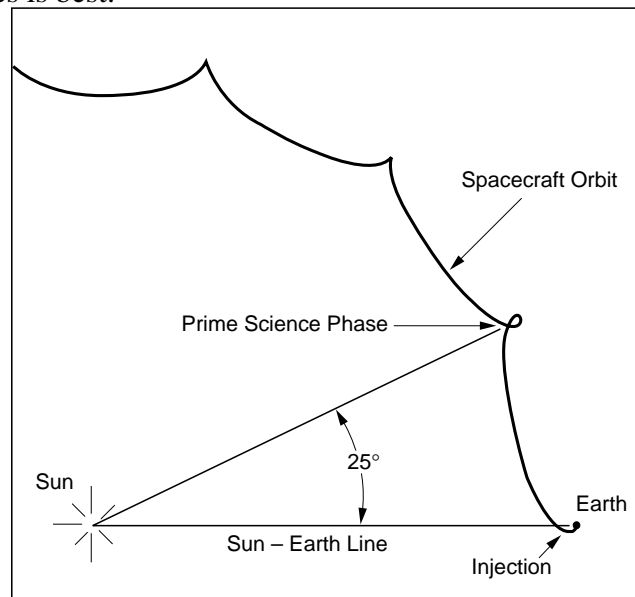

Fig. 5-1: SXCI Trajectory in rotating coordinate frame with Sun - Earth line fixed shows S/C stays near 1 AU.

Moreover, from viewing the simulated stereo SXT pairs in 3D on a SGI workstation with interlaced stereo and shuttered goggles, we found that the human brain saw coronal features as three-dimensional for stereo angles as small as a few degrees. Generally, because of the fact that most X-ray features have such short lifetimes, the best 3D viewing of simulated SXT (rotational) stereo pairs with the shuttered goggles was 6-8 hrs corresponding to 3-4° (this is the separation of the image pair on the cover of the report). From true stereo pairs such as the test loops in Fig. 3-3, we determined that the human brain reconstructs a 3D view from stereo pairs for stereo separations as large as 15° which is the human-eye stereo angle for an object held roughly 10 inches away. Therefore, for human visual interpretation of the 3D structures in the corona from stereo pairs and videos, and also for outreach and education, angles in the range 3-15° may be preferable. Thus an orbit which samples a wide range of angles, but spends more time at 25-40° where errors in quantitative 3D determination are smaller, is preferred.

The final orbit chosen for the study satisfies these requirements. A plot of the spacecraft trajectory in the Sun-Earth rotating coordinate frame is shown in Fig. 5-1. In this coordinate frame, the Sun-Earth line remains fixed and SXCI is shown drifting relative to the Sun-Earth line. The spacecraft drifts away from the Earth in a slightly elliptical (0.9 AU periapsis x 1.0 AU apoapsis) heliocentric orbit. As shown in Fig. 5-2, a stereo angle of 25° degrees is achieved 260 days after launch and remains constant (± 1°) for 160 days. This provides a stable observing environment for the collection of stereoscopic images and occurs because of the phasing of the nearly identical orbits of the Earth and spacecraft about the Sun. No additional propulsive maneuvers are needed after the initial injection into heliocentric orbit. The dwells at ~25° and ~51° seen in Fig. 5-2 result from the varying orbital velocity of the elliptical spacecraft orbit.

The baseline mission can be divided in several phases. The first 100 days could be used for check out and calibration. The mid-course phase, extending from day 100 to day 260, can be used to study the effect varying stereo angle has on image processing and stereo reconstruction. Also, data for stereo videos for analysis and outreach/education are collected here because the angles in this phase are excellent for human stereo viewing (see Sec. 4.A.1) and because the data rate is high. After the spacecraft has drifted to approximately 25° stereo angle, the 160 day prime science phase begins.
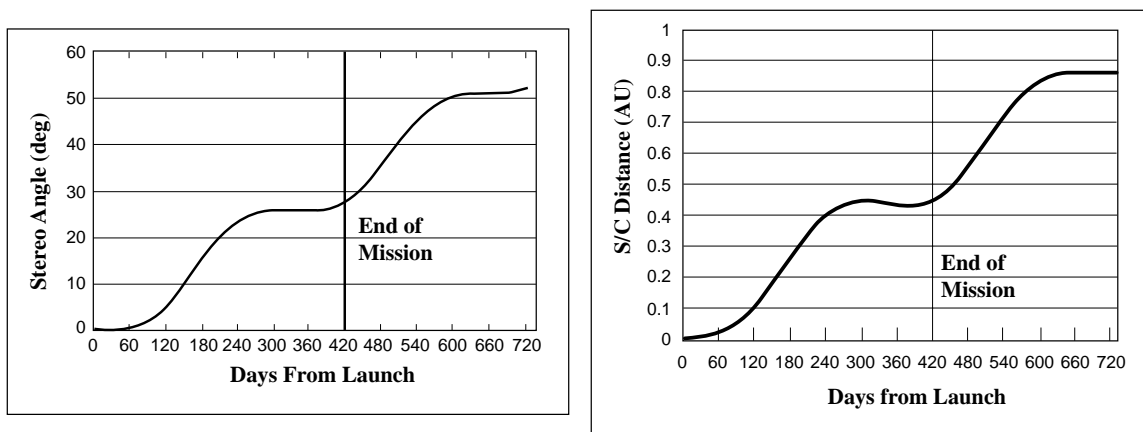

Fig. 5-2: Left: Stereo (Earth-Sun-S/C) Angle vs. Flight Time shows S/C dwells near 25° stereo angle. Right: Spacecraft distance from Earth vs. flight time.

The baseline mission costed in Sec. 8 ends at 420 days. However, if the mission is extended, the new science objectives described in Sec. 2 and Table 2-4 can be addressed when the angle is >40°. Specifically, extended longitudinal coverage of the X-ray corona is provided by the two well-separated telescopes and one begins to observe the X-ray corona underlying CMEs occurring near the limb where they are best detected by near-Earth coronagraphs.

6. The Soft X-Ray Imaging (SXI) Instrument

For the last thirty years the structure, variability and dynamics of the solar corona have been revealed through several space missions (Skylab, Yohkoh). These missions carried grazing incidence soft X-ray telescopes to image the characteristic emission of the high temperature ionized gas of which the corona is composed. In addition to revolutionizing our view of the corona, these missions demonstrated how coronal images could be used to identify and locate the sites of activity which are responsible for ejecting the particles and fields into interplanetary space which frequently disrupt the terrestrial system. From these observations, NOAA concluded that access to coronal X-ray images on a continuous basis would vastly improve their ability to forecast "space weather." The SXIs that will be included in the complement of instruments to be flown on all future GOES satellites, starting with GOES M, are the outcome of this conclusion.

At the time the first SXI was authorized by the METSAT Project Office, it was conceived as a low budget, operational instrument that would contain only commercially available hardware and would require no technological development. However, this included high performance grazing incidence optics and CCD detectors. The first SXI, developed at MSFC (Fig. 6-1), was and is viewed as a pathfinder and because it is an add-on to an existing spacecraft its design is severely constrained by the envelope available in the stowed (launch) configuration. The later GOES spacecraft will fly improved versions of the SXI instruments incorporating an advanced detector which will improve their imaging performance. The improved SXIs for GOES N, O, P, and Q will be build by Lockheed Martin, Palo Alto (selected in June 1997 under a competitive GSFC procurement). The instrument parameters for both types of SXI instruments are summarized in Table 6-1.

The first SXI telescope consists of a grazing incidence mirror, a twelve position broadband filter wheel and a focal plane assembly containing an intensified CCD camera with 5 arcsec pixels. The mirror consists of standard paraboloid hyperboloid reflecting surfaces in a Wolter I configuration fabricated from a single zerodur element. Spectral information is obtained using a 12-position filter wheel which contains 9 analysis filters which form two groups of short and long wavelength broadband filters. Four short wavelength filters (6-16 Å bandpass) are made from beryllium and five long wavelength filters (6-60 Å bandpass) from a thin film of polyimide ($C_{17}H_5O_4N_3$) coated with aluminum and titanium to exclude the visible, UV components of the solar spectrum which manage to pass through the prefilters. The latter are fabricated from similar coated polyimide film. The temperature of the emitting region is found from the ratio of the emission using one long wavelength and one short wavelength filter. This GOES-M telescope is illustrated in Fig. 6-1. Requirements levied on the spacecraft by the SXI are given in Table 6-2.
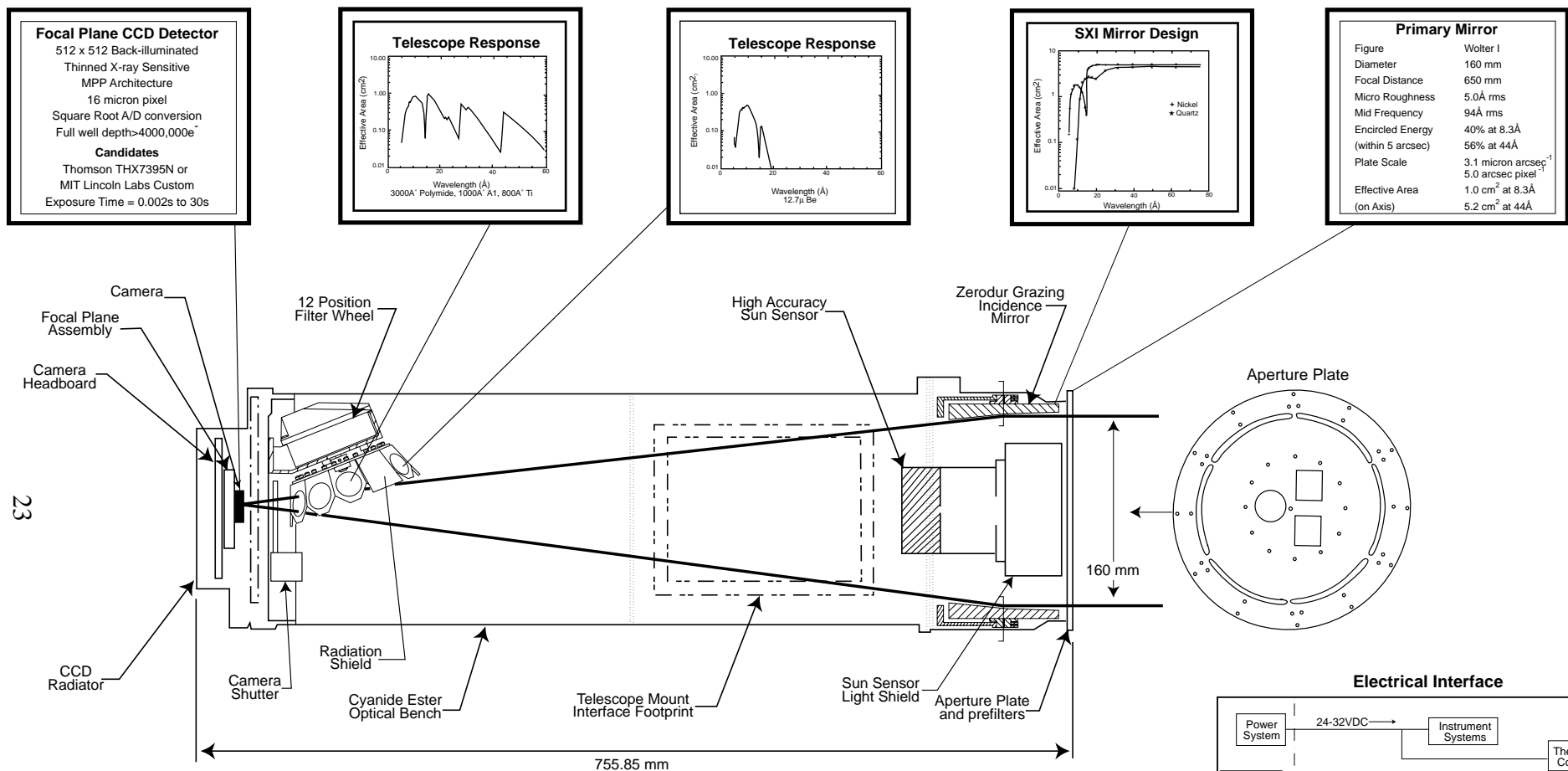
23

Focal Plane CCD Detector
512 x 512 Back-illuminated
Thinned X-ray Sensitive
MPP Architecture
16 micron pixel
Square Root A/D conversion
Full well depth>4000,000e⁻
Candidates
Thomson THX7395N or
MIT Lincoln Labs Custom
Exposure Time = 0.002s to 30s

Telescope Response
Effective Area (cm²)
Wavelength (Å)
3000Å˚ Polymide, 1000Å˚ A1, 800Å˚ Ti

Telescope Response
Effective Area (cm²)
Wavelength (Å)
12.7µ Be

SXI Mirror Design
Effective Area (cm²)
Wavelength (Å)
+ Nickel
★ Quartz

Primary Mirror
Figure	Wolter I
Diameter	160 mm
Focal Distance	650 mm
Micro Roughness	5.0Å rms
Mid Frequency	94Å rms
Encircled Energy	40% at 8.3Å
(within 5 arcsec)	56% at 44Å
Plate Scale	3.1 micron arcsec⁻¹
	5.0 arcsec pixel⁻¹
Effective Area	1.0 cm² at 8.3Å
(on Axis)	5.2 cm² at 44Å

Camera
Focal Plane Assembly
Camera Headboard
12 Position Filter Wheel
High Accuracy Sun Sensor
Zerodur Grazing Incidence Mirror
Aperture Plate
CCD Radiator
Camera Shutter
Radiation Shield
Cyanide Ester Optical Bench
Telescope Mount Interface Footprint
Sun Sensor Light Shield
Aperture Plate and prefilters
160 mm
755.85 mm

Fig. 6-1. The GOES-M Soft X-Ray Imager (SXI) Instrument

Electrical Interface

Power System
24-32VDC
Instrument Systems
Thermal Control
Spacecraft Pointing System I/F
s/c orientation data
HASS Control
HASS
Timing Logic
CCD Camera
ROM
Instrument Contoller & I/F Logic
Peripherals Filter Wheel Shutter
Video Driver
Spacecraft Contoller
Commands
Data
RAM
Signal Processing Logic
Video Mux
Spacecraft Memory
Image Data
I/F Control Logic
Image Memory
A/D
S/C
Instrument

5-30304

The SXI will be able to image density structures with temperatures in the range 1-10 MK. Although the solar corona contains material across the full temperature range, the brightest features are generally the hottest and their spectra are biased toward higher energy (shorter wavelength) photons. Standard, front illuminated, CCDs are also more sensitive to the higher energy photons in this range, which amplifies this effect and makes it difficult to resolve the cooler structures. For instance the TI (J) CCD used on Yohkoh becomes relatively insensitive below 400 eV (30Å) and in order to image the quiet corona exposure times of 15-30 s or longer are required. Because the SXI is mounted on the GOES solar array, which is continually stepped at 3 s intervals to track the Sun, the maximum exposure time for the GOES-M SXI is 3 s. Therefore, since one of the objectives of the SXI program was to observe coronal hole boundaries, which are relatively weak features, directly illuminated CCDs were rejected in favor of an intensified CCD, i.e., a combination of a microchannel plate (MCP), phosphor coated coupler and a CCD in order to enhance the sensitivity to cooler features. Since the sensitivity of an MCP is inversely proportional to energy, i.e., it is more sensitive at longer wavelengths, it acts to reduce, rather than amplify, the intrinsic dynamic range in each image.

Table 6-1. Stereo SXI Instrument Summary

	Basic SXI (GOES M)	Improved Stereo SXI (GOES N,O,P,Q)
Optics	Figure Wolter I, Nickel Coated, Zerodur	
Diameter	160 mm	160 mm
Focal Distance	650 mm	1655 mm
Micro Roughness	7.2Å rms	TBD
Mid Frequency	108Å rms	TBD
Plate Scale	3.1 micron arcsec^{-1} 5.0 arcsec pixel^{-1}	3.1 micron arcsec^{-1} 5.0 arcsec pixel^{-1}
Effective Area (on axis)	0.8 cm^2 at 8.3Å 4.8 cm^2 at 44Å	1.2 cm^2 at 8.3Å 4.8 cm^2 at 44Å
Encircled Energy (within 5 arcsec)	27% at 8.3Å 47% at 44Å	50% at 8.3Å 68% at 44Å
Focal Plane Detector	MCP HOT Device with 8 micron pores Phosphor Nichia NP1043 Taper magnification 1:1.2 CCD Thomson 512 x 512 Full well depth 450,000e	512x512, 16μ pixel back illuminated, thinned X-ray sensitive CCD Full well depth >61,000e
Exposure Time	0.002s to 3.0s	0.002 to 30s with IMC

Additional advantages of this detector are that the MCP provides electronic shuttering and that the optical coupler can be used to match the size of the telescope focal plane to the detector. The image size is set by the maximum allowable focal length of the telescope which is approximately 650 mm. This corresponds to a plate scale of 3.1 microns/arcsec or to about 5 arcsec/pixel for typical CCDs with 18-20 micron pixels. Even if CCDs with smaller pixels were available they would not necessarily be suitable for the SXI since the CCD must also provide a large dynamic range. The latter is a function of the full well depth

24

which is proportional to the area of the pixel. Consequently, improvements in the image resolution by decreasing pixel size are offset by loss of dynamic range. Finally, the lack of pointing stability of the GOES platform argued against attempts to improve resolution for the first SXI.

Table 6-2. Stereo SXI Imager Properties and Requirements

		Telescope	*Electronics*
Envelope Shape		Cylindrical	Rectangular
Size		(1.32m x 0.29m)	0.008 m^3
Weight (including Sun-sensor)		15.1 kg	6.8 kg
Power (average, includes heaters)		37 Watts	
Pointing	Accuracy	± 1 arcmin	
	Stability	1 arcsec peak to peak over 10 s.	
	Knowledge	± 1-2 arcsec	

The GOES N through Q instruments will benefit from recent technological developments in CCD manufacturing and will have an improved detector in the form of a mechanically shuttered, directly illuminated CCD. Two candidate CCDs have been identified, both of which have a suitable geometrical format. Since they are both thinned, back illuminated devices, their spectral response at long wavelengths is expected to be greatly improved over both the TI(J) device used on Yohkoh and the GOES-M microchannel plate. Both candidate CCDs are 3-phase devices and it is proposed to use this feature to implement on-chip image motion compensation (IMC) by shifting the columns back and forth in response to a pointing error signal generated by the high accuracy Sun sensor. Such an approach is well suited to the GOES environment where the pointing instability occurs predominantly in the E-W direction.

A contract for the GOES N through Q SXI instruments has been placed by the GOES Project Office with Lockheed Martin and the first improved SXI should be in orbit circa 2001. Consequently we have chosen to baseline the SXCI mission using improved SXIs for both elements of the stereo pair, i.e. the Earth orbiting and the interplanetary telescopes. If it is decided to proceed with the SXCI program, the interplanetary instrument could be fabricated alongside the GOES SXIs since the design requirements for instruments flying in geosynchronous or interplanetary orbits are very similar. Such an approach would enable the SXCI telescope to be acquired at a competitive price, estimated to be in the range of $12-14M.

7. Spacecraft and Launch Vehicle

In this section, the SXCI spacecraft and launch vehicle are described and results of related trade studies reported. The SXCI spacecraft concept meets all functional requirements while minimizing cost and risk by using a combination of design simplicity, extensive design heritage, and generous performance margins. The spacecraft + instrument dry mass is 129 kg. A Pegasus XL is used to place the spacecraft in Earth orbit and a solid rocket

motor then injects it into the ~1 AU drifting heliocentric orbit described in Sec. 5. The spacecraft cost is estimated to be $17.3M.

7.A   Spacecraft Configuration

Figure 7-1 shows front and back views of the spacecraft external arrangement in its post-injection configuration. The spacecraft is approximately 1150 mm (45.3") in diameter by 2131 mm (84.0") high. It weighs about 129 kg after injection when the solid rocket motor (SRM) propellant has been depleted.

Key features shown include:

- The cylindrical solar array ensures adequate power generation during all mission phases and Sun angles and during the downlinks. This design approach was chosen to avoid the need to deploy or articulate the array, increasing reliability and minimizing jitter during operation of the imager. The medium gain antenna (MGA) is mounted below the array using a short mast. The cylindrical axis of the spacecraft defines the spacecraft X-axis.

- The flat cylindrical sunshield/radiator is mounted above the array to shield the units mounted on the equipment shelf and the SXCI instrument from direct sunlight. Holes in the sunshield accommodate the SXCI instrument and star tracker fields of view (FOV's) and the radial thrusters. The cylindrical portion of the shield acts as a radiator to dissipate heat deposited in the equipment shelf.

- The SXCI payload (the X-ray telescope) is mounted on the equipment deck inside the sunshield to allow a clear view of the Sun (through the aperture in the sunshield/radiator) and to provide a clear radiator FOV for focal plane cooling. The instrument boresight defines the spacecraft's +Z axis.

- The 608x608 mm (24.0x24.0") diameter high gain antenna (HGA) array which is mounted to the top of the sunshield/radiator. The spacecraft slews about its cylindridal (X-) axis to point the HGA at Earth for downlinks. When not pointed to Earth, the HGA doubles as a solar sail (see section 7.2.1).

- Four 0.045 N axial thrusters are mounted two each on the + and - X faces as shown. They operate with six 0.045 N and two 6.8 N radial thrusters that fire through holes in the array to provide three axes of rotation and translation for vehicle attitude control and despin.

- The nozzle of the Star-27 G solid rocket motor (SRM) can be seen beneath the bottom edge of the solar array. The SRM is not separated after burnout to avoid the complexity of a separation system. Heat soakback following the burn is minimized by using a titanium attach fitting for the SRM.

1. Spacecraft Functional Architecture

The SXCI spacecraft subsystems have been chosen for simplicity to reduce mass and increase reliability. The functional configuration is summarized in the top level system block diagram shown in Figure 7-2.

The limited range of Sun distances (0.9-1.0 AU) allows use of thoroughly conventional spacecraft power, thermal control and command and data handling (C&DH) subsystems. Electrical power is provided by a direct energy transfer system chosen for low weight and maximum design heritage from Ball's LOSAT-X spacecraft. The relatively constant Sun range allows a simple, fixed array and straightforward temperature control using MLI and a belt-type radiator panel that wraps around the spacecraft above the solar array. Make-up heaters replace louvers for lower cost and mass. C&DH functions are handled by a RAD-6000 based microcomputer which minimizes mass by offloading hardware functions to massless software. Subsystem interfaces are simplified by the MIL-STD-1553B data bus, further reducing mass and cost. The spacecraft's functional architecture is specifically optimized for the SXCI mission.

The Attitude Determination and Control subsystem (ADCS) uses coarse Sun sensors, and a Wide Field of View star tracker to provide attitude determination in all modes. In addition, the fine Sun sensor included as part of the SXCI instrument provides 1 arcsecond accuracy attitude knowledge during imaging. As the primary attitude control reference, the star tracker provides spacecraft attitude in 3 axes with 30 arcsecond accuracy (3σ) at a 5 Hz rate. Attitude control is provided by a single 2.3 N-m-s momentum wheel using a momentum bias approach. The wheel's angular momentum vector is oriented and the wheel is unloaded by the RCS subsystem describedbelow. When not pointed to Earth, the HGA doubles as a solar sail, helping to bring the vehicle's center of (solar) pressure as close as possible to its center of gravity (CG) to minimize solar torques and RCS propellant consumption. Software running in the C&DH processor accomplishes all attitude determination and control computations, sequencing and thruster control.

The SXCI telecommunications subsystem operates at X-band through the Deep Space Network (DSN) 34 m HEF (high efficiency) net to receive commands, downlink telemetry and provide tracking for navigation. The data rate during the prime mission phase (at 0.45 AU) is 70 kbps. Our design approach was chosen for maximum heritage to reduce risk. It uses low, medium and high gain antennas, a Small Deep-Space Transponder and a 22W TWTA X-band power amplifier. The functional arrangement of these components is shown in Fig. 7-2; the antenna locations and orientations are shown in Fig. 7-1. The telecommunications link performance is summarized in Sec. 7.A.3 (see also Fig. 7-6).

A Ka band downlink was also investigated. Although capable of providing approximately four times the downlink data rate for a given Earth range, e.g. over 200 kpbs at 0.5 AU, we rejected it for reasons of increased cost (particularly for the spacecraft antenna) and the limited availability of compatible DSN ground stations (NASA presently has only a single 34m ground station capable of receiving Ka band signals, and no firm plans for adding any more).

To maximize operational flexibility, the spacecraft is equipped with a 22 Gbit Erasable Disc Mass Memory, allowing storage of many days of data between downlinks. This provides the operational flexibility needed to minimize operations costs and DSN Scheduling constraints. The use of this large mass memory during operations is discussed in Sec. 8.A.

The Propulsion/Reaction Control Subsystem (P/RCS)needs to provide 3252 m/sec of delta-V for heliocentric orbit insertion. In its RCS role, The P/RCS needs to furnish about 500 N-s of RCS impulse to despin the vehicle after heliocentric orbit insertion and to provide

the attitude control functions described above. These requirements are met by a solid rocket motor (SRM) and by a simple cold gas system. The SRM is a development of the off-the-shelf STAR-27 which uses a graphite-epoxy case and a reinforced carbon-carbon nozzle to reduce inert mass and increase specific impulse to 293 seconds. The nitrogen cold gas RCS uses twelve .045 N thrusters and two 194 mm pressurant tanks, and, except for the .045N thrusters, uses 100% off-the-shelf components to reduce cost and risk.

2. Spacecraft Hardware Heritage

SXCI hardware heritage is high to reduce both cost and risk. Figure 7-3 is a pie chart that shows the percentages of SXCI hardware that are either new, flight qualified, or flight proven. These categories are defined as follows:

(a) Flight Proven: 47% of the SXCI equipment complement falls into this category. Flight proven hardware is identical to units that have flown on other spacecraft. Flight proven equipment used on the SXCI spacecraft includes the Power Control Unit, the batteries, the star tracker, most RF components, and all Propulsion/RCS subsystem components except the thrusters.

(b) Flight Qualified: 14% of the SXCI equipment is flight qualified. This category covers existing, qualified hardware developed for programs with flight dates prior to the ~2001 SXCI launch date. Examples of this category include the DSN transponder and the valve drive electronics which will fly early next year on Ball's GFO spacecraft.

(c) New: 39% of SXCI equipment consists of developmental units or of the integrating elements normally mission peculiar or configuration dependent. Integrating element components in this category use strictly conventional materials and design approaches and include the solar array (assembled from existing, flight proven cells); the secondary structure; wire harness, coax cables, MLI blankets, and RCS subsystem lines and fittings. All of these items are standard builds; none of them represents a schedule or development risk. Only the .045 N thrusters used by the RCS are considered to developmental items.

61% Flight qualified and proven hardware will directly reduce cost by eliminating non-recurring engineering effort. Development risk will be eliminated as the performance of these heritage items is already verified.

3. Spacecraft Performance Margins

Large performance margins are included to further reduce risk. Figures 7-4, 7-5 and 7-6 summarize the generous mass, electrical power, and telecommunications link performance margins available to our spacecraft concept.

We have provided a generous mass margin by using the Pegasus XL launch system (see Sec. 7.B). Figure 7-4 presents a preliminary breakdown of the spacecraft mass by subsystem. Masses were estimated by similarity and by using masses of existing components when possible, and for the most part should be conservative. The dry mass of the spacecraft plus instrument is 129.1 kg. A blanket 20 % growth contingency has been added for the spacecraft engineering subsystems. This contingency, combined with the

13% margin on mass at separation, indicates that the spacecraft will be a low risk development.

 The power subsystem performance by mode is summarized on Fig. 7-5 which shows a breakdown by subsystem for the spacecraft's two primary operational modes. The resulting end-of-life (EOL) worst-case power margin is 14 %. This margin at EOL combined with the 20% electrical power contingency shown also indicates a very low risk development.

The performance of the SXCI telecommunications links is summarized in Fig. 7-6, which shows available uplink and downlink bit rates as a function of the spacecraft antenna used and the range to the Earth. Link margins, antenna coverage and gains used are also shown. The generous 7.6 dB margin available for the hi-rate downlink will further reduce risk.

4. Spacecraft Cost

We have estimated costs for the SXCI Spacecraft using Ball's standard estimating process which is well anchored to previous program costs and experience to provide good accuracy. Our estimated cost is $17.3 M. This cost is in FY97 dollars and includes Ball's fee.

The scope of our estimate includes design, development, production, bus level integration and test, integration of the SXCI payload (costed separately), system testing of the assembled spacecraft and integration of the spacecraft to the launch vehicle. No mission operations costs or support are included and there is no deliverable ground support equipment associated with this effort. These costs are included in the total mission cost estimate given in Sec. 9.

7.B Launch Vehicle

We have selected the Pegasus XL launch vehicle for SXCI because of its combination of throw weight performance and fairing envelope, which simplifies packaging of the spacecraft. Figure 7-7 shows a side view of the SXCI spacecraft integrated inside the enhanced Pegasus XL fairing envelope. The fairing volume allows elimination of spacecraft deployments. The spacecraft mounts to the Pegasus using a spacecraft supplied Payload Attach Fitting (PAF) which is mounted to the top of the fixed SRM adapter and which incorporates a spacecraft supplied but launch system actuated marmon clamp separation system used to separate the SXCI spacecraft after spin-up.

7.C   Impact of Mission Orbit Circularization

We conducted a brief study to determine the impact of circularizing the baseline elliptical SXCI orbit, which would leave it in a 1 AU circular orbit at a fixed angular separation from Earth. Results show that the increase in spacecraft startburn mass in low Earth Orbit (LEO) required for circularization will require use of a higher performance launch vehicle such as the Lockheed-Martin Athena I or Orbital Science Corporation Taurus XL, instead of the cheaper, but less capable, Pegasus XL. This alone increases the total mission cost by about $9M.

1. Requirements: When the spacecraft reaches a specified Earth-Sun-spacecraft angle (the stereo angle viewing angle), circularize the orbit to hold or "freeze" this angle. To calculate the needed delta-V, we assumed an initial elliptical "drifting" orbit with a period of 395 days and assumed the specified Earth-Sun-spacecraft angle was 30 degrees. When the spacecraft completes its first orbit, 13 months have passed, and the spacecraft lags 30 days (and 30 degrees) behind the Earth, providing the specified separation. To "freeze" the spacecraft at this 30 degree separation, it must be decelerated by 752 m/s as it passes the perigee point in its orbit. This turns the elliptical orbit back into a circular orbit at a radius of 1 AU, locking the separation angle at 30 degrees.

2. Implementation Trades: We looked at monopropellant (hydrazine), bipropellant (monomethyl hydrazine and nitrogen tetroxide) and solid rocket motor (SRM) propulsion options for applying the 752 m/s circularization delta-V. Because of its low specific impulse (Isp), monopropellant hydrazine increased the mass of the spacecraft beyond even the throw weight limits of the higher performance launch vehicle options considered; therefore, we dropped it from further consideration. The Biprop and SRM options came out virtually equivalent in performance, with the SRM option significantly (about a factor of four) cheaper. Either option can be launched by a higher performance launch vehicle such as the Lockheed-Martin Athena I, the Orbital Science Corporation Taurus XL, or a SELV-II class vehicle, as described in the recent Small Explorer Class Mission (SMEX) Announcement of Opportunity. We chose the SRM approach because of its lower cost.

Table 7-1. Impact of Orbit Circularization on Spacecraft Design

#	Change Item	Mass Impact (kg)	Comments
1	**Baseline SXCI S/C, dry**	**129**	Starting point
2	Augment structure	+33	To accommodate new SRM's
3	Add Star 30C SRM inert mass	+57	For injection into initial elliptical orbit
4	Add Star 13 A SRM inert mass	+10	For circularization delta-V
5	Delete Star 24G SRM inert mass	-25	Replaced by larger Star 30C
6	**Totals**	**204**	**New dry weight**
7	RCS pressurant	+6	Spin-up; spin-down; 3 year RCS
8	Circularization propellant	+65	For two Star 13 SRM's; 752 m/s delta-V
9	Injection propellant	+583	For Star 30C SRM; 3250 m/s delta-V
10	**Total, SXCI S/C @ separation**	**858**	**113% increase over Baseline S/C**
11	S/C to launch vehicle adapter	+24	Includes separation system
12	**Total mass on LV**	**882**	
13	SELV-II throw weight	1000	to 185 km parking orbit @ i = 28 deg.
14	Margin	118	
15	Margin on mass at separation	13%	

3. Spacecraft design impact: Starting with the baseline spacecraft, we needed to make the changes summarized in Table 7-1 to allow orbit circularization.

4. Circularization Cost Impact: All of these changes are feasible, and involve low levels of risk. The additional cost of adding the Star-13 SRM's and changing to the larger Star 30C will need to be assessed, and added to the cost of the larger higher performance SELV-II class launch system. Based on launch vehicle costs given in the 1997 SMEX Announcement of Opportunity, the increased cost of the higher performance SELV-II class vehicle over a SELV-I class vehicle (e.g, a Pegasus) would be on the order of $9M.

8. Mission Operations and Ground System

8.A Data and Observation Strategies for Maximum Science Return

Since this is a deep-space imaging mission, data return and telemetry are major issues. In addition to the usual data compression strategies, the SXCI mission can use a unique new strategy for maximizing the science return by taking advantage of the simultaneous observations of the Sun from the GOES telescope. The basic concept is to store much more imaging data on board than can be downlinked; data from periods of interest are then selectively downlinked. From the GOES (or alternatively coronagraph) data, the times at which CMEs or other eruptive events of interest occurred can be determined and thus which portion of the SXCI imaging data are of most interest and should be marked for downlinking. Using this strategy, high cadence data from the build-up, initiation and explosive phases of CMEs or other eruptive events can be selectively downlinked. This data strategy requires that mission operations include scientists monitoring the GOES X-ray or other data on an almost daily basis.

To implement this strategy, we sized the on-board memory at 22 Gbits. This does not cause a large mass or cost penalty because 10-20 Gbit erasable disk mass memory devices weighing about 5 kg are now available for about $500K. The memory has been sized to accommodate several days of data. A normal full disk image requires 12 bits per pixel and is composed of 512x512 pixels for 3 Mbits per image. Hence, the on board disk can hold approximately 7000 full disk images before it begins to overwrite itself. Data would be recorded at a much higher cadence than 1 Gbit per day. Specifically, data could be recorded at a high enough cadence to observe the complete evolution of CMEs and flares. Scientists would monitor the GOES and other near-Earth observations daily and determine which portions of the data should be downlinked and which portions should be marked for deletion. This information is uplinked to the spacecraft during the scheduled uplink/downlink periods. Since the data can remain on the recorder for several days before being downlinked, this strategy can be implemented within a low cost 40-hour/week mission operations schedule with several downlink periods per week. Only with both the large on-board storage and the knowledge of the event times from near-Earth observations is this strategy made possible.

The Deep Space Network 34 meter antennas are used to communicate with the spacecraft, using X band frequencies. The downlink from the spacecraft contains science data as well

as engineering, instrument, and navigation data. The antenna is fixed, so the spacecraft rotates to turn the antenna towards Earth for communications.

Observation sequences would consist of a core program plus objective driven specific campaigns, i.e., CME and flare patrols, active region heating studies, etc. Images will be recorded either as full disk (core program) or partial disk images and stored in the spacecraft's on-board memory. A baseline observation program was developed for the prime mission phase that consists of a core program plus four programs that have specific objectives but which require either an enhanced cadence, a restricted field of view or both. The core program (full disk coverage) allows us to study the gradual evolution of the corona to study the buildup of energy that may be the cause of both heating and eruptive events. A CME patrol (full disk coverage) follows the rapid evolution of the corona immediately prior to the event, during the event, and afterwards. The flare patrol (50% disk coverage) performs the same function for flares. This is made possible by the on board data handling strategy, which allows us to store high cadence data on board and, using the GOES observations, to selectively send back data of interest.
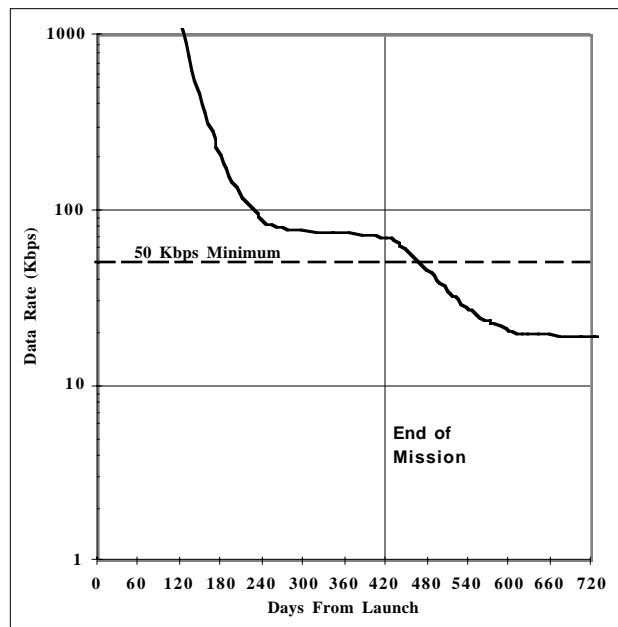

Fig. 8-1. SXCI Mission Data Rate vs. Flight Time shows data rate ≥ 50 Kbps with 3 db margin during SXCI mission

The data rate during the prime mission phase (~0.45 AU from Earth) is approximately 70 kbps. We estimate that about 720 hours of 34m Deep Space Network (DSN) time would be used to cover the three mission phases: near Earth (100 days), a mid-course (160 days), and prime mission (160 days) phases with about 480 hours used for the prime phase when the data rate is lower. During the prime science phase (23 weeks), the spacecraft could downlink data 3 times a weeks for a total weekly data volume of about 5 Gbits (~1700 images/week) and a total prime phase volume of 120 Gbits or 39,000 images. The total data volume from the mid-course phase would be 49 Gbits or 16,000 images assuming 182 hours of DSN time for this phase.

The data rate as a function of distance is given in Fig. 8-1. The much higher data rate early in the Mid-Course Phase (1 Mbytes/sec at 125 days) is especially useful for downlinking high cadence sequences of images to be used for outreach and education as well as qualitative "by human eye" analysis of coronal structures and dynamics since this is when the stereo angle is optimum for human 3D visualization of stereo pairs (See Sec. 5). More specifically, high cadence image sequences for 3D IMAX movies would be obtained in this phase.

8.B   Ground System

The ground system baselined for this mission (Fig. 8-2) is based on the use of existing JPL Advanced Multi-Mission Operations System (AMMOS) capabilities, including hardware, software, and operations personnel. Because the SXCI spacecraft has only one science instrument (which is always Sun pointed except during downlinks) and a large onboard data storage capacity for flexibility, the ground system can be operated by an 8-person team working normal business hour, keeping operations costs low.
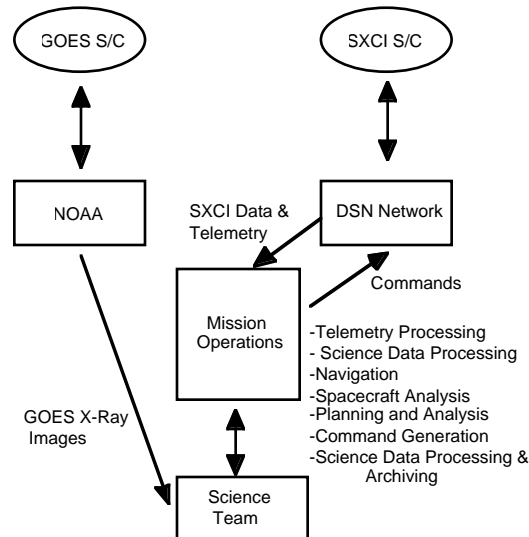

Fig. 8-2. SXCI Ground System Block Diagram shows flow of science and engineering data and S/C commands.

The ground system, shown in Fig. 8-2, consists of 7 subsystems: Planning and Analysis, Command Generation, Telemetry Processing, Navigation, Spacecraft Analysis, Science Data Processing and Archiving and the Deep Space Network (DSN). The Planning and Analysis subsystem integrates science data requests with spacecraft and instrument data requests from the Spacecraft Analysis team to produce a schedule of events for the Command Generation subsystem to process and convert into spacecraft commands. The downlink process returns science data and engineering telemetry from the spacecraft via the DSN to the Telemetry Processing subsystem. This subsystem processes the data and provides the Orbit Determination data to the Navigation subsystem, provides the spacecraft and instrument engineering data to the Spacecraft Analysis subsystem, and provides science data to a Science Data Processing and Archiving subsystem. This is the ground system used in the cost estimate given in Sec. 9.

33

9. Mission Cost

A first-order cost estimate was produced using a combination of grassroots and analogy methods, according to assumptions and guidelines specified in the SMEX Announcement of Opportunity issued April, 1997. These include a cost for DSN time of $1.6K/hour. The total mission cost was estimated to be $78.4M in $FY97 assuming a launch in September 2000. All of the various mission components (orbit, mission profile, spacecraft, ground system, etc.) are as described in the preceding sections. Costs for such this as management and overhead use JPL costs. Also, JPL overhead on the instrument and spacecraft subcontracts has been included.

Table 9-1 gives a breakdown of various components of the cost estimate called out in the SMEX Announcement of Opportunity in $FY97. Included is a reserve of 20% on the spacecraft in Phases A/B/C/D and 15% on the instrument and ground system development. Phase E begins at Launch + 30 days and includes operations, science data analysis and $1.2M for outreach. Costs for the Pegasus launch vehicle were assumed to follow the profile shown for the "Small Class (Fairing A)" launch vehicle shown in Table D-2 of the SMEX Announcement of Opportunity. Table 9-2 gives a breakdown of the Phase A/B/C/D and Phase E costs separately. The science costs in these phases before data are obtained reflects the need for the development of analysis and visualization tools for the stereoscopic X-ray data. $10M has been allocated to science data analysis in Phase E.

Table 9-1. SXCI Mission Costs in $FY97M

Phases A/B/C/D	42.2
Ground System Development	2.9
Phase E(Launch + 30 days)	14.4
Launch Vehicle & Services	19.0
TOTAL	78.4

Table 9-2. Cost Breakdown for Phases A/B/C/D and Phase E in $FY97M

	A/B/C/D	E
Project Management	1.6	0.6
Science	1.8	10.0
Outreach	0.4	1.2
Operations & Mission Design	0.7	2.6
Spacecraft (includes JPL overhead on subcontract)	18.3	0
Instrument (includes JPL overhead on subcontract)	14.0	0
Reserves	5.4	0
TOTAL (Phases A/B/C/D)	42.2	14.4

References

Alexander, D. and Katsev, S., 1996, Solar Phys., 153, 153

Antiochos, S. K., 1997, "Theories of Coronal Mass Ejections," EOS 78, Vol. 78, No. 46 Supplement, F575.

Berton, R., and Sakurai, T., 1985, Solar Phys., 96, 93.

Craig, I. J. D., McClymont, A. N., & Underwood, J. H. 1978, A&A, 70, 1

Feynman, J., and. Martin, S. F.: 1995, *J. Geophys Res.*, 100, 3355.

Forbes, T. G., & Acton, L. W. 1996, ApJ, 459, 330

Gary, G. A., 1997a, Solar Phys., August, (in press).

Gary, G. A., Davis, J. M., and Moore, R.: 1997b, Solar Phys. "Comments On Solar Stereographic Missions For The Analysis Of Coronal Plasma Structures" (submitted)

Gosling, J. T., 1993, *J. Geophys Res.,* 98, 18,937.

Isenberg, P.A., Forbes, T.G., and Demoulin, P., 1993, *Astrophys. J.*, 417, 368.

Kano, R., and Tsuneta, S. 1995, ApJ, 454, 934

Kano, R., and Tsuneta, S. 1996, PASJ, 48, 535

Klimchuk, J. A. 1992, in Coronal Streamers, Coronal Loops, and Coronal and Solar Wind Composition, ed. V. Domingo, J. Mariska, & A. Poland (ESA Pub SP-348), 167

Klimchuk, J. A., and Porter, L. J., 1995, Nature, 377, 131

Liewer, P. C., Davis, J. M., De Jong, E. M., Klimchuk, J. A., Reinert, R., Davila, J. M., and Feynman, J., 1997, "Stereo X-Ray Corona Imager: Report on New Mission Concept Study," EOS, 78, S255.

Lorre, Jean, De Jong, E. M., Ingersol, A., 1997 (private communication).

McClymont, A. N., Jiao, L, and Mikic, A., (1997) "Problems and Progress in Computing three-dimensional coronal active region magnetic fields from boundary data," (submitted).

Mikic, Z., 1997 (private communication).

Mikic, Z. and Linker, J. A., 1994, Ap. J., 430, 898.

Mikic, Z. and McClymont, A., 1994, "Deducing Coronal Magnetic Fields from Vector Magnetograms," in *Solar Active Region Evolution: Comparing Models with Observations*, (Balasubramaniam, K.S., and Simon, G. W, eds., ASP conference Series, Vol. 68) 225.

Moore, R. L, Schmieder, B., Hathaway, D. H., and Tarbell, T. D., 1997,"3-D Magnetic Field Configuration Late in a Large Two-Ribbon Flare." (MSFC Report).

Parker, E. N. 1983, ApJ, 264, 642.

Parker, E. N. 1988, ApJ, 330, 474.

Pevtsov, A., Canfield, R. C., and Zirin, H., 1996, ApJ, 473, 533.

Porter, L. J., and Klimchuk, J. A., 1995, ApJ, 454, 499.

Rosner, R., Tucker, W. H., & Vaiana, G. S., 1978, ApJ, 220, 643.

Rust, D. M. and Kumar, A., 1994, ApJ, 464,L199.

Shimizu, T., Tsuneta, S., Acton, L. W., Lemen, J. R., and Uchida, Y. 1992, PASJ, 44, L147.

Shimizu, T. et al., 1994, ApJ, 422, 906

Space Studies Board, National Research Council, *A Science Strategy for Space Physics*, (National Research Council, Washington, D.C, 1995), p.3

Vesecky, J. F., Antiochos, S. K., & Underwood, J. H., 1979, ApJ, 233, 987